Remote Sensing of Precipitation on the Tibetan Plateau Using the TRMM Microwave Imager

ZHANYU YAO

Laboratory for Severe Storm Research, Department of Geophysics, Peking University, and Chinese Academy of Meteorological Sciences, Beijing, China

WANBIAO LI, YUANJING ZHU, BOLIN ZHAO, AND YONG CHEN

Laboratory for Severe Storm Research, Department of Geophysics, Peking University, Beijing, China

(Manuscript received 14 July 2000, in final form 20 November 2000)

ABSTRACT

The Tibetan Plateau is a unique location for studying the global climate and China's severe weather. The precipitation on the Tibetan Plateau can be studied conveniently with the Tropical Rainfall Measuring Mission (TRMM) Microwave Imager (TMI). It is shown that the TMI brightness temperature at 85 GHz in the vertical polarization (TB_{85V}) is negatively correlated to the surface rain rate, but a very low value of TB_{85V} does not correspond to very intense surface rain rates on the Tibetan Plateau, a result that is different from what is observed in other areas of the world. For surface precipitation retrieval on the Tibetan Plateau from TMI, the effect from snow cover on precipitation retrieval is removed before analysis of precipitation. Using the dynamic cluster *K*-mean method, five categories of surface types and rain areas are identified on the Tibetan Plateau: dry soil, wet soil, water area, stratiform rain area, and convective rain area. The precipitation areas are screened by classification before the precipitation retrieval. Two datasets of rain-free areas and precipitation areas are formed after surface classification. Based on the dataset of rain-free areas, the value of TB_{85V} can be simulated well by TB_{10V}, TB_{19V}, and TB_{21V} when it is not raining. By means of the dataset of precipitation areas, it is revealed that the scattering index over land (SI_L) is positively correlated and the polarization-corrected brightness temperature at 85 GHz (PCT_{85}) is negatively correlated with the surface rain rate. With SI_L, PCT_{85}, and their combinations as retrieval algorithms, three precipitation retrieval formulas are proposed in which the SI_L algorithm is most suitable for small rain retrieval, the PCT_{85} algorithm is most suitable for moderate rain retrieval, and the combined SI_L and PCT_{85} algorithm is most suitable for relatively large rain retrieval on the Tibetan Plateau. By means of two thresholds, 265 and 245 K, for TB_{85V}, the combination of the three formulas is applied to precipitation retrieval on the Tibetan Plateau during the Tibetan Plateau Experiment Intensive Observing Period of 1998, resulting in acceptable and encouraging surface rain-rate retrievals. Intercomparison among the TMI algorithms and the 17 Special Sensor Microwave Imager algorithms from the second Precipitation Intercomparison Project demonstrates that the comprehensive application of the TMI algorithms has good precision and error index and is suitable for precipitation retrieval on the Tibetan Plateau.

1. Introduction

The Global Energy and Water Cycle Experiment (GEWEX) of the World Climate Research Program has been ongoing since 1988. The GEWEX activities in China were initiated in 1991. In 1998, four important GEWEX–related projects were carried out in China simultaneously. They are the Tibetan Plateau Experiment (TIPEX), South China Sea Monsoon Experiment, Huaihe River Basin Experiment (HUBEX), and South China Heavy Rainfall Experiment. Among the four experiments, TIPEX was carried out on the Tibetan Plateau, for which the study of precipitation was one of the highest priorities.

Because of its unique characteristics of high elevation, complex surface condition, and climate environment, the Tibetan Plateau has an important effect on the climate and its change in China, Asia, and, perhaps, worldwide. It is also an important factor to Chinese severe weather research. However, there are very few weather stations, so very little meteorological and climate information exists on this vast plateau. The severe weather conditions and complex terrain make it impossible for direct meteorological observation over a large portion of the plateau. Satellite measurements offer an opportunity to understand better the weather and the climate of this region. In this paper, data from the Tropical Rainfall Measuring Mission (TRMM) Microwave

Corresponding author address: Dr. Zhanyu Yao, Chinese Academy of Meteorological Sciences, 46 Zhong Guan Cun South Street, Beijing 100081, China.
E-mail: yaozhanyu@263.net

© 2001 American Meteorological Society

Unauthenticated | Downloaded 04/24/24 07:19 AM UTC

TABLE 1. Spatial resolution for each channel of TMI (channel 21.3 GHz is in the vertical polarization, and the other channels are in dual polarization).

Frequency (GHz):	10.7	19.4	21.3	37.0	85.5
Spatial resolution (km):	38.3	18.4	16.5	9.7	4.4

Imager (TMI) are used to retrieve precipitation on the Tibetan Plateau.

2. Data analysis

a. TMI data

The TRMM satellite was launched jointly by the United States and Japan in November of 1997 with the primary purpose of observing tropical rainfall from space. It scans for 15.77 orbits daily between 40°N and 40°S latitude. TMI is one of the two rainfall sensors on the satellite. In comparison with the Special Sensor Microwave Imager (SSM/I) on the satellites series of the U.S. Defense Meteorological Satellite Program, TMI has higher spatial resolution because of the lower orbit of the TRMM satellite. Thus, it has a better capacity to monitor mesoscale and small-scale precipitation systems. The addition of 10.65-GHz dual polarization channels allows for more penetration to the earth's surface. Table 1 shows spatial resolution for each channel of TMI.

b. Surface precipitation data

During the TIPEX Intensive Observing Period (IOP) 1998 (May–August 1998), surface observations and radiosonde observations were carried out simultaneously in the open or at weather stations on the Tibetan Plateau. Because of the severe and complex weather and surface conditions, there were very few observation sites. In this paper, surface precipitation data from four observing sites (stations) from 1 June to 31 August 1998 are used, the latitudes (N) and longitudes (E) of which are (30.480°, 91.100°), (31.100°, 97.267°), (31.150°, 97.167°), (33.750°, 99.650°). Figure 1 offers examples of the surface rain rate data from two observing sites, Changdu (31.100°N, 97.267°E) and Dangxiong (30.480°N, 91.100°E), during TIPEX/IOP 1998.

3. Relationship between TMI TB_{85V} and surface rain rate

According to our data analysis, 85 GHz-V (V represents vertical polarized) is the most sensitive TMI channel to the surface rain rate on the Tibetan Plateau. Figure 2 presents the simple relationship between the brightness temperature of 85 GHz-V (TB_{85V}) and the surface rain rate (RR) without consideration of effects from any other TMI channels. The scatterplot is based on the TMI data and the surface RR data at four observing sites (stations) on the Tibetan Plateau from 1 June to 31 August 1998.

From Fig. 2, we can see that TB_{85V} is negatively correlated to the surface RR. When the values of RR are less than 3 mm h^{-1}, the corresponding values of TB_{85V} are generally greater than 265 K. For RR between 3 and 5 mm h^{-1}, the corresponding TB_{85V} mainly drop into the range between 265 and 245 K. The corresponding TB_{85V} of those points with RR greater than 5 mm h^{-1} are basically less than 245 K. From the scatterplot, we also find that a very low value of TB_{85V} does not correspond to very intense surface RR on the Tibetan Plateau, a result that is different from what is observed in other areas of the world.

4. Precipitation retrieval from TMI

a. Data match

To match TMI data to surface observation data at the same time and place during TIPEX/IOP 1998, we selected TMI data over the Tibetan Plateau with latitudes 26°–39°N and longitudes 77°–100°E from 1 June to 31 August 1998.

b. Removing the effect of snow cover

On the Tibetan Plateau, some places are covered with snow most of the year. The effect of snow cover must be removed when we retrieve the surface precipitation area from TMI. Snow cover was first derived from passive microwave remote sensing in 1972 (Kunzi et al. 1976). With more channels available, some improved snow cover retrieval algorithms have been proposed (Kunzi et al. 1984; Chang et al. 1990). When the 85-GHz channel from SSM/I is considered, snow cover can be detected more accurately; however, interference from precipitation and other potential false signatures must be considered (Grody 1991; Grody and Basist 1996; Ferraro et al. 1996).

With the measurements of nine channels from TMI, we can also detect and screen the snow cover similarly on the Tibetan Plateau among various potential signatures. We can follow the four steps below to detect snow-cover areas on the Tibetan Plateau using the method of Grody and Basist (1996).

1) IDENTIFICATION OF SCATTERER (SCAT)

To describe the scattering signature of snow cover for individual TMI fields of view (FOV), the differences of brightness temperatures (TB, K) at low and high frequencies should be considered. If SCAT = max [(TB_{21V} − TB_{85V}), (TB_{19V} − TB_{37V})] ≥ 5, snow cover may be present. Otherwise, no snow cover exists.

Unauthenticated | Downloaded 04/24/24 07:19 AM UTC

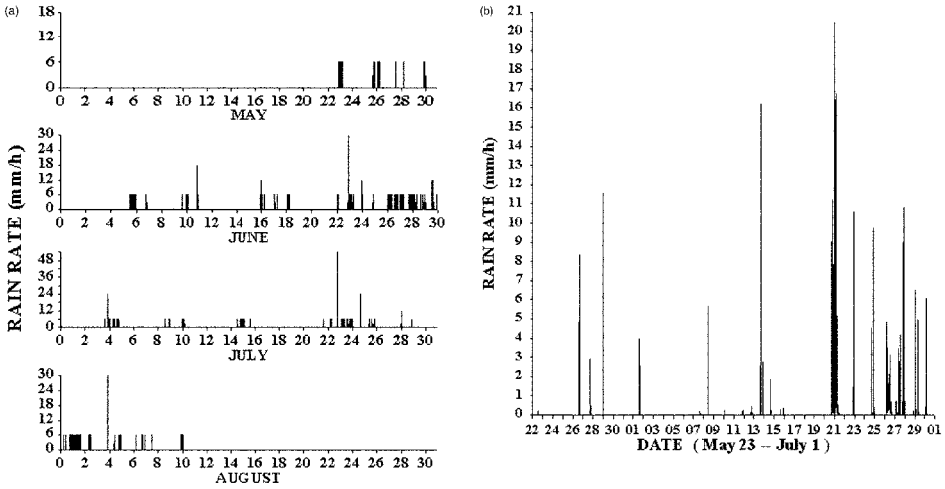

FIG. 1. Daily surface RR data from two observing sites: (left) Changdu (31.100°N, 97.267°E) and (right) Dangxiong (30.480°N, 91.100°E).

2) IDENTIFICATION OF PRECIPITATION

Sometimes the signatures for precipitation and the ones for snow cover are difficult to separate. Here, the following factors are used to screen precipitation from snow cover. If $TB_{21V} \geq 265$, or $TB_{21V} \geq 169 + 0.50TB_{85V}$, or $261 \leq TB_{21V} \leq 265$ and $SCAT \leq 6$, it should be identified as precipitation area. Otherwise, snow cover may be present.

3) IDENTIFICATION OF COLD DESERT

For cold desert identification, the following factors are considered. If $TB_{19V} - TB_{19H} \geq 18$, and $TB_{19V} - TB_{37V} \leq 14$, and $TB_{37V} - TB_{85V} \leq 10$, it should be identified as cold desert area. Otherwise, snow cover may be present.

4) IDENTIFICATION OF FROZEN GROUND

To identify frozen ground, the following factors are available. If $TB_{19V} - TB_{19H} \geq 8$, and $TB_{19V} - TB_{37V} \leq 6$, and $TB_{21V} - TB_{85V} \leq 10$, it should be identified as frozen ground area. Otherwise, snow cover may be present.

After these four steps of identification, the FOV of TMI is assigned to snow-covered areas on the Tibetan Plateau, and we can remove the effect of snow cover before our precipitation retrieval.

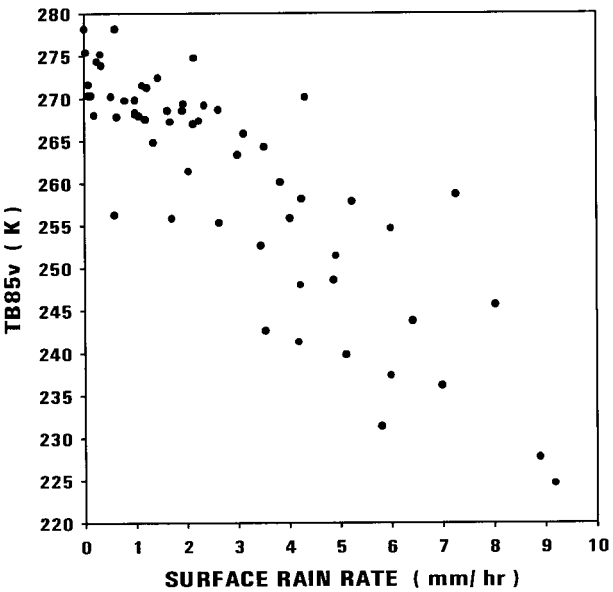

FIG. 2. Simple relationship between TB_{85V} and surface RR.

c. Identification of precipitation area

The earth's surface is a strong emitter of radiation, and the surface emissivity is one of the main factors to determine the quantity of surface radiation. Several researchers (Spencer 1986; Spencer et al. 1989; Neale et al. 1990; Grody 1991; Fiore et al. 1992) proposed empirical criteria to classify the earth's surface. In this study, a dynamic cluster *K*-mean method is used to discriminate five categories of surface types and rain areas on the Tibetan Plateau: dry soil, wet soil, water area, stratiform rain area, and convective rain area.

A category center is defined by the mean value of similar samples. The distance between a sample and a certain category center is called the distance between this sample and the category. For the initial classification, the square sum of the distances between each category center and the corresponding internal samples is named as the classification error. The aim of the cluster method is to find a kind of classification with the classification error as small as possible while the initial classification has been assigned. For this reason, all sam-

Unauthenticated | Downloaded 04/24/24 07:19 AM UTC

ples are checked one by one to determine if they belong to a nearest category. Those samples that do not belong to the nearest category will be assigned to the nearest category to reduce the classification error, and the category center will be regulated at the same time. By repeating the process above, the smallest classification error can be obtained, and the classification is determined ultimately.

To classify the five categories successfully on the Tibetan Plateau, seven factors are applied in this study for the cluster analysis: TB_{85V}, TB_{85H}, TB_{37V}, TB_{37H}, TB_{21V}, TB_{19V}, and TB_{19H}.

Figure 3 provides an example of the comparison between a cluster classification image and the corresponding images by TMI TB_{85V} and the TRMM Visible and Infrared Scanner (VIRS) TB-channel 5 (Ch5; 12 μm). Figure 3a offers an image of classification with the map of Tibetan Plateau by means of the dynamic cluster *K*-mean method above. The TMI data of seven channels were used for the classification over the Tibetan Plateau with latitudes 26°–39°N and longitudes 77°–100°E from 1539:57 to 1545:44 UTC 16 June 1998. The five grayscales from black to white in the figure represent the five categories of surface types and rain areas (dry soil, wet soil, water area, stratiform rain area, and convective rain area). Figure 3b gives the corresponding image from TMI TB_{85V}, in which the whiter the grayscale is, the lower the TB_{85V}. Figure 3c presents the corresponding image by VIRS TB-Ch5, in which the whiter the grayscale is, the lower the TB-Ch5.

As we know, TB_{85V} is very sensitive to scattering by ice crystals at the upper part of cold clouds. The lower the TB_{85V} is, the more intense the scattering by the ice crystals. That is to say, a relatively low value of TB_{85V} usually results in surface rain. Sometimes some warm clouds also lead to surface rain, but no or few ice crystals exist. This means that a relatively warm TB_{85V} can sometimes exist when rain occurs at the surface. So, we have reason to believe that the actual surface rain areas are often more than and larger than the areas of low values of TB_{85V}. Now let us compare Fig. 3a with Fig. 3b. The convective rain areas (with the whitest grayscale) in Fig. 3a are consistent with the areas with low values of TMI TB_{85V} (with relatively white and bright grayscales) in Fig. 3b, especially on the east part of the two images. The stratiform rain areas (with the second-whitest grayscale) in Fig. 3a and some convective rain areas on the west part of the image are more and larger than the corresponding areas in Fig. 3b, meeting the analysis above.

Figure 3c is an infrared cloud chart by VIRS-Ch5 (12 μm). Several convective cloud clusters (with white and bright grayscales) are evidently shown on the east part of the image, the places of which are in accordance with the convective rain areas (with the whitest grayscale) on the east part of Fig. 3a, but the areas of which are larger than the ones in Fig. 3a. This is reasonable, because the edges of convective cloud clusters are often not accompanied by surface rain. There are some stratiform clouds mixed with some convective clouds and some clouds of other forms on the west and in central parts of Fig. 3c, the areas of which are larger than the stratiform rain areas (with the second-whitest grayscale) and convective rain areas (with the whitest grayscale) in Fig. 3a. This is also reasonable, because stratiform clouds are not always accompanied by surface rain, the same as for the clouds of other forms. So, we have reason to believe that the actual surface rain areas are usually fewer and smaller than the areas of clouds in the corresponding cloud chart.

It is a pity that because of the lack of weather stations on the Tibetan Plateau, we have no actual data of surface types and raining areas as validation of our classification results during TIPEX/IOP 1998. From the comparison of Fig. 3 and the analysis above, however, we have reasons to believe that the cluster classification result in Fig. 3a is reasonable and acceptable.

Figure 4 shows the relationship between each category of the five classification types and the combination of TB_{19V} and TB_{37V} after the classification using the dynamic cluster *K*-mean method at 1539:57–1545:44 UTC on 16 June 1998. The scatterplot is similar to the result from Rao et al. (1990, p. 271, chap. VII-6).

From Fig. 3 and Fig. 4, we can see that the classification of surface types and rain areas on the Tibetan Plateau based on the dynamic cluster *K*-mean method is feasible. By using the dynamic cluster *K*-mean method, the precipitation areas on the Tibetan Plateau are identified and screened before our precipitation retrieval.

d. Precipitation retrieval algorithms

Among the studies on scattering precipitation retrieval algorithms, Spencer (1986, 1989) proposed two algorithms using the combinations of the difference between brightness temperatures of two different polarized channels, for 37 GHz and 85 GHz, respectively. Liu and Curry (1992) put forward a precipitation retrieval algorithm with contribution of both absorption and scattering. Grody (1991) suggested the scattering index as a precipitation retrieval algorithm. On the basis of Grody's algorithm, Ferraro and Marks (1995) brought forward an improved precipitation retrieval algorithm using a scattering index classified by land and ocean.

Because of the differences of orbit height, incident angle, and microwave channels between TMI and SSM/I, a new precipitation retrieval algorithm suitable for TMI should be applied. In this study, three TMI precipitation retrieval algorithms are proposed and have been applied to our precipitation retrieval on the Tibetan Plateau.

1) SCATTERING INDEX

The scattering index is used to estimate the scattering intensity by ice crystals in the atmosphere. Usually, the

Unauthenticated | Downloaded 04/24/24 07:19 AM UTC

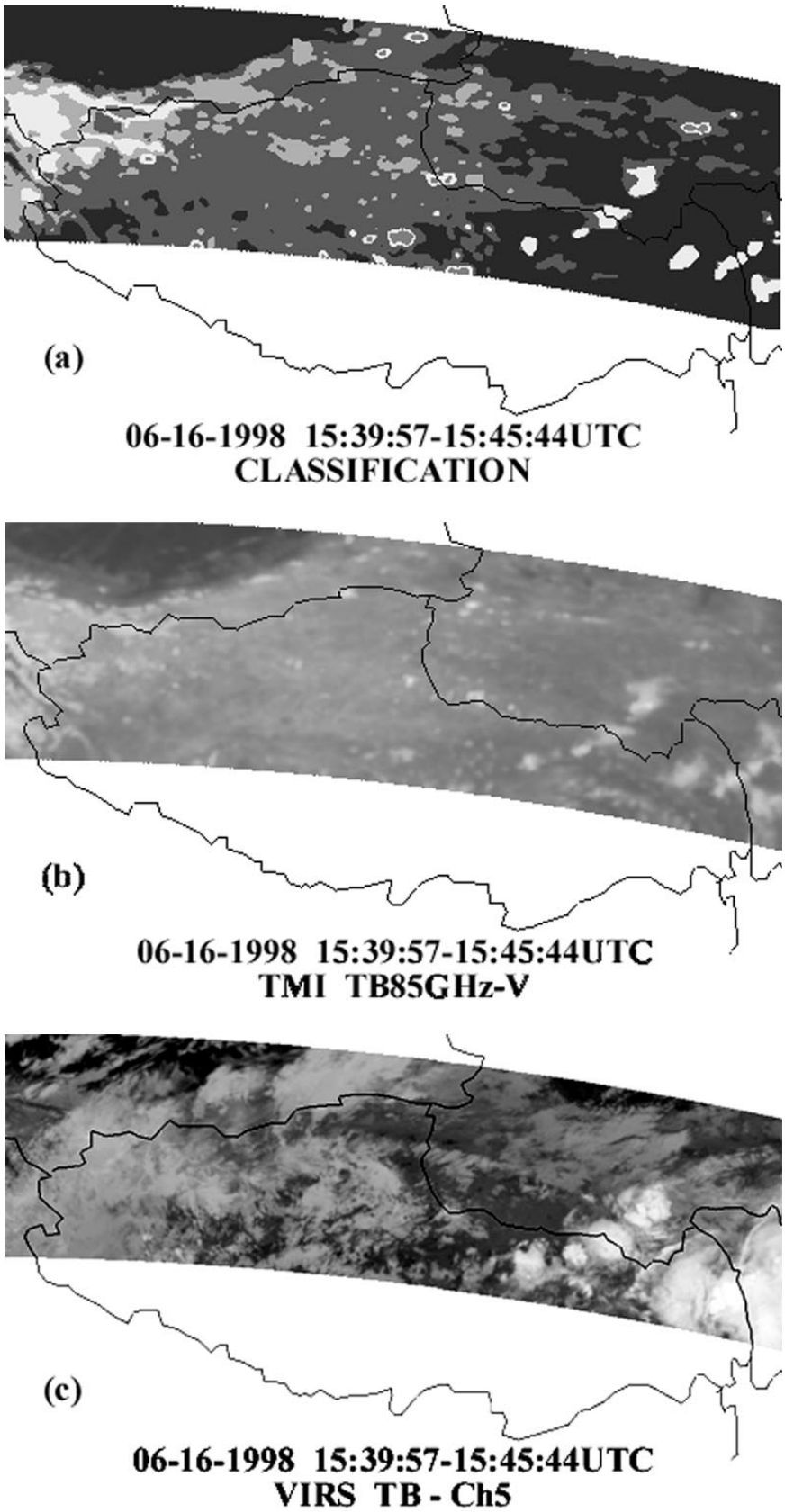

FIG. 3. Comparison between a cluster classification image and the corresponding images by TMI TB_{85V} and VIRS TB-Ch5.

Unauthenticated | Downloaded 04/24/24 07:19 AM UTC

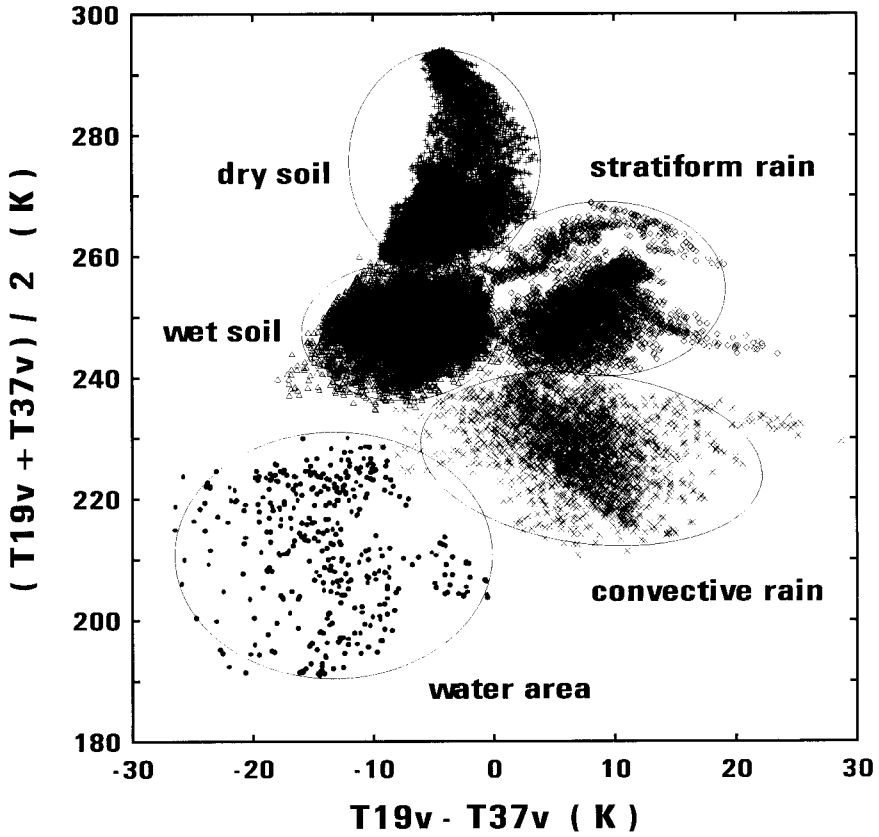

FIG. 4. Relationship between each category of the five classification types and the combination of TB_{19V} and TB_{37V}.

TBs at high-frequency channels are highly affected by ice-crystal scattering, while the TBs at low-frequency channels are not. If there is no effect from ice-crystal scattering in the atmosphere (rain-free weather), the TB at a high-frequency channel (usually TB_{85V}) can be simulated well by the TBs at low-frequency channels (e.g., TB_{10V}, TB_{19V}, and TB_{21V}). When ice-crystal scattering exists (raining weather), the difference between the simulated value of TB_{85V} by the TBs at low-frequency channels and the actual value of TB_{85V} is used to determine the scattering intensity by ice crystals in the atmosphere.

To derive the scattering index, the simulation formula of TB_{85V} by the TBs at low-frequency channels first must be given out. For this purpose, we chose those points that belong to the category of dry soil after the classification of five categories described above, and we formed the dataset of rain-free areas. Those points belonging to the categories of stratiform rain area and convective rain area were selected to be formed as the dataset of precipitation areas.

With nine channels of TMI, we named $E(10V, 19V, 21V)_{85V}$ as the estimated value of TB_{85V} by TB_{10V}, TB_{19V}, and TB_{21V}. Based on the dataset of rain-free areas, we regressed a formula of $E(10V, 19V, 21V)_{85V}$ as follows, which was used to estimate the value of TB_{85V}:

$$E(10V, 19V, 21V)_{85V} = -65.487 - 0.1862TB_{10V} - 0.454\,56TB_{19V} + 1.860\,47TB_{21V}. \quad (1)$$

Figure 5 presents the relationship between $E(10V, 19V, 21V)_{85V}$ and TB_{85V} under the condition of rain-free weather. From the scatterplot, we can see that, when it is not raining, $E(10V, 19V, 21V)_{85V}$ can represent well the value of TB_{85V}.

We name SI_L as the atmospheric scattering index over land, and SI_L is defined as the difference between $E(10V, 19V, 21V)_{85V}$ (the estimated value of TB_{85V}) and TB_{85V} (the observed value of TB_{85V}):

$$SI_L = E(10V, 19V, 21V)_{85V} - TB_{85V}. \quad (2)$$

In the rain-free areas, the SI_L should be zero or very small. When SI_L is applied to the precipitation areas, it represents the scattering intensity of radiation energy at 85 GHz-V by the precipitating atmosphere. The larger the SI_L is, the more intense the scattering and the heavier the precipitation.

Equation (2) tells us that SI_L is negatively correlated to TB_{85V} when it is raining. Because of the negative correlation between TB_{85V} and RR (Fig. 2), we know that SI_L must be positively correlated to the surface RR.

Unauthenticated | Downloaded 04/24/24 07:19 AM UTC

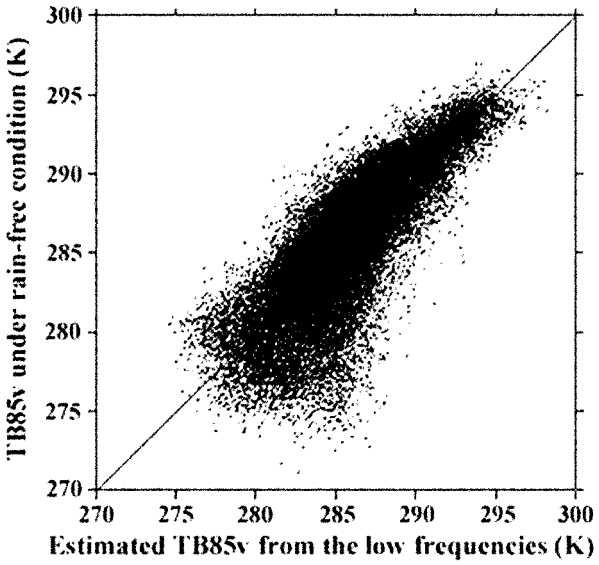

FIG. 5. Simulation of TB_{85V} by means of $E(10V, 19V, 21V)_{85V}$ under the condition of rain-free weather.

2) POLARIZATION-CORRECTED BRIGHTNESS TEMPERATURE AT 85 GHZ

Another factor sensitive to surface precipitation is polarization-corrected brightness temperature at 85 GHz (PCT_{85}). Spencer et al. (1989) gave a formula of PCT_{85} as follows:

$$PCT_{85} = 1.818TB_{85V} - 0.818TB_{85H}. \quad (3)$$

The formula above was derived on the basis of examination of several days of SSM/I observations of global cloud-free oceanic areas. According to Spencer et al. (1989), absolute accuracy for β [ratio of TB_V warming to TB_H warming; see Spencer et al. (1989)] is not as important as keeping it constant. Thus in our precipitation retrieval, we choose the mean value of $\beta = 0.45$ suggested by Spencer et al. from which Eq. (3) was derived. Our purpose here is to determine if the PCT_{85} defined as Eq. (3) is a sensitive factor in our precipitation retrieval.

Equation (3) shows that PCT_{85} is positively correlated to TB_{85V} when it is raining. Because TB_{85V} has a negative correlation to RR (Fig. 2), we know that PCT_{85} must be negatively correlated to the surface RR.

3) THREE PRECIPITATION RETRIEVAL ALGORITHMS

By the analysis above, we know that both SI_L and PCT_{85} have a good relationship with surface RR, so we can set up precipitation retrieval algorithms by means of SI_L, PCT_{85}, and their combinations.

Because there are very few precipitation data of surface observation on the Tibetan Plateau, we cannot generate precipitation retrieval algorithms on the basis of the surface date in this area. To generate our algorithms, we applied the TMI data and the surface radar observation data from HUBEX, which was carried out in China at the same time that TIPEX was done. Out purpose here is to determine if the algorithms derived from HUBEX data can be applied to the Tibetan Plateau after some adjustments or under some conditions.

TABLE 2. Accuracy statistics for the regressions of the three retrieval formulas.

Retrieval equations	Samples	Correlation coefficient	Rms (mm h^{-1})
Eq. (4)	3578	0.570	1.585
Eq. (5)	3578	0.616	1.519
Eq. (6)	3578	0.658	1.453

By means of regressions with 3578 samples from HUBEX data, we put forward three precipitation retrieval formulas on the basis of SI_L, PCT_{85}, and their combinations:

$$RR = 0.864 + 0.069\,33SI_L \quad (4)$$

$$RR = 39.090 - 0.131\,62PCT_{85} \quad (5)$$

$$RR = 124.236 - 0.429\,06PCT_{85} - 0.343\,18SI_L \quad (6)$$

In the three formulas above, RR (mm h^{-1}) is surface rain rate. Table 2 offers accuracy statistics for the regressions of the three formulas above. Figures 6a–c show the relationships between the surface radar observed RR and the RRs retrieved by the SI_L algorithm, PCT_{85} algorithm, and combined SI_L and PCT_{85} algorithm, respectively.

e. Application result of the three algorithms and discussion

We applied the three algorithms above to our precipitation retrieval on the Tibetan Plateau based on the TMI data and the surface precipitation data at four observation sites (stations) from 1 June to 31 August 1998. All of the samples that met the conditions of data match for time and space were used for RR calculation. Equations (4), (5), and (6) were used to calculate RR_1, RR_2, and RR_3, respectively, for each sample. It was revealed that $RR_1 < RR_2 < RR_3$ for all of these samples. That is to say, when applying the three algorithms above on the Tibetan Plateau, the retrieval value by the PCT_{85} algorithm [Eq. (5)] is larger than the one by the SI_L algorithm [Eq. (4)] and smaller than the one by the combined SI_L and PCT_{85} algorithm [Eq. (6)].

In comparing the RR_1, RR_2, and RR_3 with the surface observed RR (RR_{obs}) for all of the retrieval samples on the Tibetan Plateau, we found that RR_1 was most close to RR_{obs} when RR_{obs} was small (usually < 3 mm h^{-1}), RR_2 was most close to RR_{obs} when RR_{obs} was moderate (usually 3–5 mm h^{-1}), and RR_3 was most close to RR_{obs} when RR_{obs} was large (usually > 5 mm h^{-1}). The comparison results tell us that, on the Tibetan Plateau, the SI_L algorithm is most suitable for small rain retrieval, the PCT_{85} algorithm is most suitable for moderate rain

Unauthenticated | Downloaded 04/24/24 07:19 AM UTC

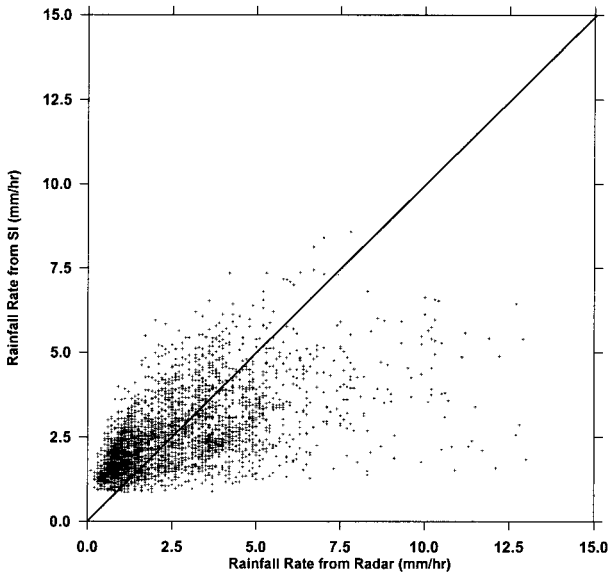

(a)

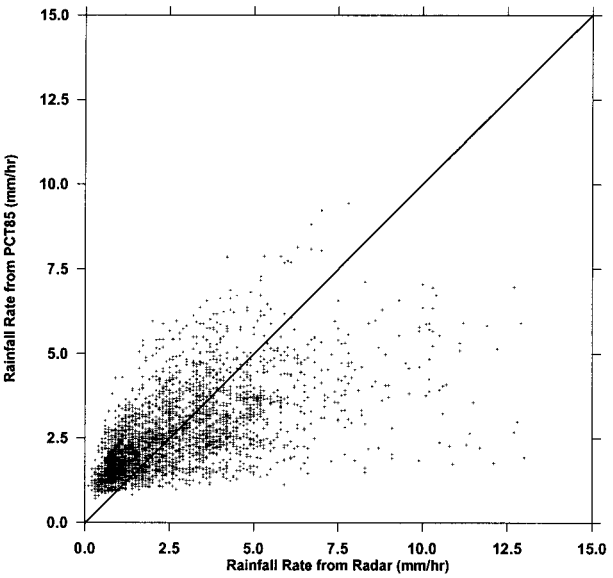

(b)

FIG. 6. Relationships between the surface radar observed RRs and those derived from the three precipitation retrieval algorithms: (a) SI_L algorithm, (b) PCT_{85} algorithm, and (c) combined SI_L and PCT_{85} algorithm.

retrieval, and the combined SI_L and PCT_{85} algorithm is most suitable for relatively large rain retrieval.

According to the results of Fig. 2, we know that, on the Tibetan Plateau, generally speaking, $TB_{85V} \geq 265$ K when RR_{obs} is small (usually < 3 mm h^{-1}), 245 K $\leq TB_{85V} < 265$ K when RR_{obs} is moderate (usually 3–5 mm h^{-1}), and $TB_{85V} < 245$ K when RR_{obs} is large

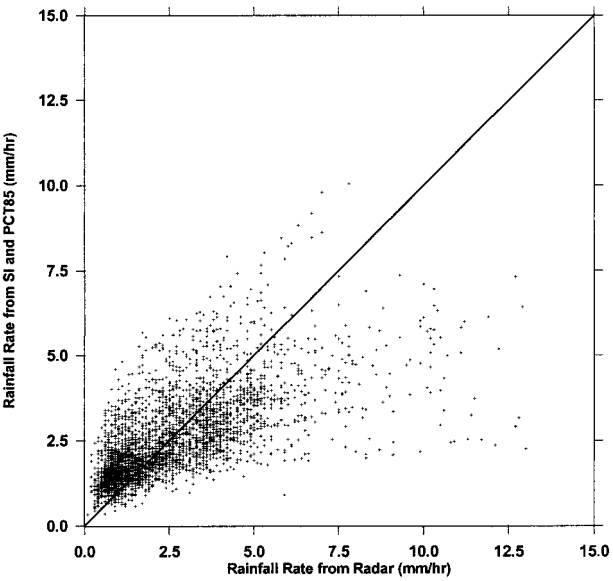

(c)

FIG. 6. (*Continued*)

(usually > 5 mm h^{-1}). Therefore, we set two thresholds, 265 and 245 K, for TB_{85V} in our precipitation retrieval on the Tibetan Plateau, and Eq. (4) was applied when $TB_{85V} \geq 265$ K, Eq. (5) was applied when 245 K $\leq TB_{85V} < 265$ K, and Eq. (6) was applied when $TB_{85V} < 245$ K. The retrieval results based on the comprehensive application of Eqs. (4)–(6) using the two thresholds above are shown in Fig. 7.

Table 3 provides the error statistics for the three TB_{85V} categories ($\geq$265 K, 245–265 K, and $<$245 K) and the comprehensive application of the three shown in Fig.

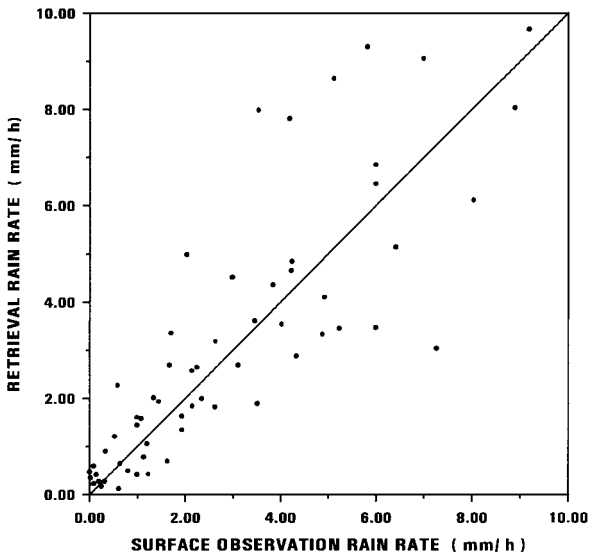

FIG. 7. Comparison between retrieval RR and surface observation RR on the Tibetan Plateau from 1 Jun to 31 Aug 1998.

Unauthenticated | Downloaded 04/24/24 07:19 AM UTC

TABLE 3. Error statistics for the three TB_{85V} categories and the comprehensive application.

TB_{85V} categories (Algorithm applied)	No. samples	Mean validation (mm h^{-1})	Mean retrieval (mm h^{-1})	Mean bias (mm h^{-1})	Rms error (mm h^{-1})	Correlation coefficient
$TB_{85V} \geq 265$ K (SI_L)	35	1.15	1.38	0.23	0.80	0.78
245 K $\leq TB_{85V} < 265$ K (PCT_{85})	13	3.95	4.32	0.37	1.84	0.56
$TB_{85V} < 245$ K (combined SI_L and PCT_{85})	12	6.75	6.60	−0.15	2.30	0.76
Comprehensive application	60	2.88	3.06	0.18	1.47	0.85

7, which include the number of samples, mean validation (mean value of surface observed RR), mean retrieval (mean value of retrieved RR), mean bias (difference between mean retrieval and mean validation), rms error, and correlation coefficient. From Fig. 7 and Table 3 we can see that the result is encouraging, based on the limited surface data we have obtained and have used.

To estimate our TMI algorithms for RR retrieval objectively, we compared our TMI algorithms with those used in the second Precipitation Intercomparison Project (PIP-2; Smith et al. 1998). Table 4 gives comparison statistics of our TMI algorithms and the 17 SSM/I algorithms from PIP-2 for instantaneous RR retrieval. The compared contents shown in Table 4 include mean validation data of RR (surface observation for our TMI algorithms and radar estimation and/or surface observation for the algorithms from PIP-2), mean retrieval RR by algorithms, mean bias (mean retrieval minus mean validation), ratio of mean bias (ratio of mean bias to mean validation), and rms error and correlation coefficient between retrieval and validation.

From the comparison statistics, we can see that the ratio of mean bias, rms error, and correlation coefficient from our TMI algorithms are good. Note that the retrieval results from our TMI algorithms were based on the regional datasets, but those from the other 17 SSM/I algorithms were on the basis of the PIP-2 datasets. Although some statistic values may lack persuasion for comparison because of the different datasets and area conditions, the statistical results can still present an objective estimation. It is demonstrated that the comprehensive application of our TMI algorithms is suitable for precipitation retrieval on the Tibetan Plateau.

f. Error analysis

The errors of our precipitation retrieval come from five sources.

1) *Nonuniqueness of measurements.* As we know, the information obtained from TB of TMI represents various contributions from atmosphere and earth surface under the FOV. Any change from the surface and atmosphere will affect these measurements. Because surface and atmospheric effects cannot be separated, it is difficult to obtain a unique relation between TB from TMI and the surface precipitation.
2) *Incomplete correspondence between TB from TMI and surface precipitation.* Because the FOV size from TMI can sometimes be much larger than raincell size, especially for small convective systems,

TABLE 4. Comparison statistics of different algorithms for instantaneous rain rate retrieval.

Algorithm	Mean validation (mm h^{-1})	Mean retrieval (mm h^{-1})	Mean bias (mm h^{-1})	Ratio of mean bias	Rms error (mm h^{-1})	Correlation coefficient
Our TMI algorithms applied on the Tibetan Plateau						
Comprehensive application	2.88	3.06	0.18	0.06	1.47	0.85
17 SSM/I algorithms from PIP-2 for land case						
CALVAL	3.44	0.86	−2.58	−0.75	4.14	0.21
BAUER	3.70	1.00	−2.70	−0.73	4.30	0.19
KUM	3.70	1.12	−2.58	−0.70	4.33	0.20
MRI	3.46	1.42	−2.04	−0.59	4.46	0.20
GSFC	3.62	2.44	−1.18	−0.33	5.46	0.14
OLSON	4.00	1.88	−2.12	−0.53	5.15	0.09
IFA-SAP	3.58	2.40	−1.18	−0.33	5.82	−0.07
GPROF	3.11	2.77	−0.34	−0.11	4.45	0.22
GSCAT	3.26	3.28	0.02	0.01	5.10	0.22
MSFC	3.39	3.08	−0.31	−0.09	5.09	0.25
FSU	3.80	3.69	−0.11	−0.03	5.79	0.04
FER-AVE	3.15	3.00	−0.15	−0.05	4.57	0.26
NESDIS	3.25	3.24	−0.01	0.00	5.26	0.22
PETTY	2.97	3.17	0.20	0.07	4.59	0.22
LIU-CUR	3.14	4.43	1.29	0.41	5.45	0.21
BRIS	3.20	4.14	0.94	0.29	5.35	0.27
KIDD	3.03	5.09	2.06	0.68	6.92	0.27

Unauthenticated | Downloaded 04/24/24 07:19 AM UTC

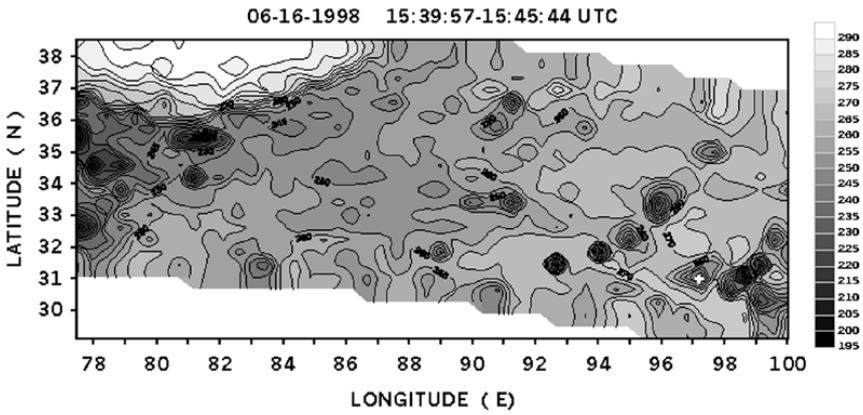

FIG. 8. The contour of TMI TB_{85V} over the Tibetan Plateau at 1539:57–1545:44 UTC 16 Jun 1998.

the precipitation signal may not be strong enough to be detected completely by TMI.

3) *Data match error*. The TMI scans for 15.77 orbits daily. Over a special area, such as the Tibetan Plateau, it is very difficult for the TB from TMI to correspond well to the surface precipitation at the same time and place. Considering the large spatial resolution for each TMI channel, the mean information within the area for one pixel of TMI does not indicate the surface precipitation completely at the site we select.
4) *Observation error of surface precipitation.* The surface precipitation data may sometimes include observation error.
5) *Application error of algorithms.* Because of the very few surface observation data on the Tibetan Plateau, we applied our TMI algorithms based on HUBEX data. The basic surface conditions and atmospheric conditions between the HUBEX area and the Tibetan Plateau are different, and this difference leads to the application error of algorithms.

5. Example analysis

Figure 8 presents the contour of TB_{85V} of TMI over the Tibetan Plateau at the time from 1539:57 to 1545:44 UTC 16 June 1998. For contrast, we demonstrate a cloud chart from channel infrared 1 (10.5–11.5 μm) of Geostationary Meteorological Satellite *GMS-5* at 1530 UTC 16 June 1998, with the Tibetan Plateau on its left-bottom part (Fig. 9).

In Fig. 8, there are several low-TB_{85V} center areas on the east part of Tibetan Plateau. These same areas appear in the cloud chart of *GMS-5* (Fig. 9) with corresponding cloud clusters over them (white areas on the east part of Tibetan Plateau; left-bottom part of the figure). Usually, the intense convective cloud cluster is accompanied by surface precipitation, and the lower the TB_{85V} is, the heavier the surface precipitation.

Now let us see a single site, Changdu (31.100°N, 97.267°E) from the two figures. In Fig. 9, Changdu (with black "+" on the east part of the Tibetan Plateau) was covered by an intense convective cloud cluster, which might lead to a heavy surface rain. From Fig. 8, we can obtain that the TB_{85V} at Changdu (with white "+") is 237 K. Because it was less than the 245 K, the combined SI_L and PCT_{85} algorithm [Eq. (6)] was applied to calculate RR, and the retrieval result was 6.84 mm h^{-1}. Actually, at the same time in Changdu, the surface observed RR was 6.00 mm h^{-1}. This result is encouraging for RR retrieval over land.

The very low value of TB_{85V} (237 K) does not correspond to a very intense surface RR on the Tibetan Plateau. This result is very different from what is observed in other areas of the world. The explanation for this phenomenon is that the atmosphere is usually very dry and the solar radiation is very intense on the Tibetan Plateau, so much evaporation of rain occurs before it reaches the ground.

6. Conclusions

We have shown that the TMI TB_{85V} is negatively correlated to the surface RR on the Tibetan Plateau, similar to what it is in most other areas. Corresponding to a certain surface RR, however, the TB_{85V} over the Tibetan Plateau is much lower than that in most other areas of the world. Despite tremendous scattering at 85 GHz, the surface precipitation is not very intense on the Tibetan Plateau. This result is mainly because of the dry atmosphere and intense solar radiation in this area and because there is much evaporation of the rain before it reaches the ground.

Data match and snow-cover removing were two important stages in our TMI algorithm development. The TMI data were carefully matched with the surface observation data according to time and place, and the effect of snow cover, which is a special characteristic on the Tibetan Plateau and can affect precipitation retrieval

Unauthenticated | Downloaded 04/24/24 07:19 AM UTC

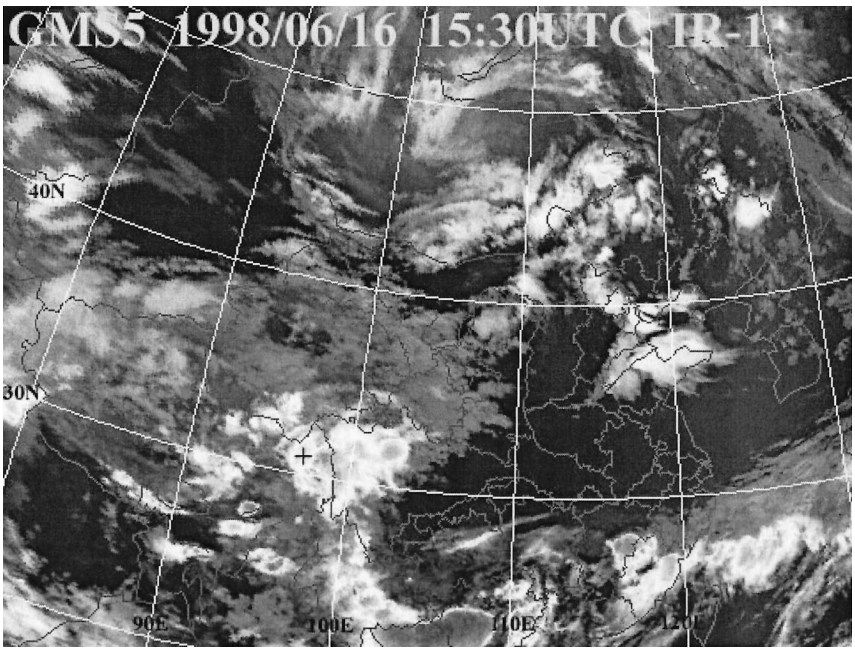

FIG. 9. Cloud chart from IR-1 (10.5–11.5 μm) of *GMS-5* at 1530 UTC 16 Jun 1998.

heavily, was removed before the analysis of precipitation.

Using the dynamic cluster *K*-mean method, we have identified five categories of surface types and rain areas on the Tibetan Plateau: dry soil, wet soil, water area, stratiform rain area, and convective rain area. It has been demonstrated that the classification of five categories is feasible. The precipitation areas on the Tibetan Plateau were screened before the precipitation retrieval.

Two datasets of rain-free areas and precipitation areas were formed after surface classification. Based on the dataset of dry soil, $E(10V, 19V, 21V)_{85V}$ can estimate well the value of TB_{85V} when it is not raining. Derived on the basis of the dataset of precipitation areas, SI_L is negatively correlated with TB_{85V} when it is raining so that it is positively correlated with the surface RR. It is also demonstrated that the positive correlation between PCT_{85} and TB_{85V} makes PCT_{85} negatively correlated with the surface RR.

With SI_L, PCT_{85}, and their combinations as retrieval algorithms, three precipitation retrieval formulas derived on the basis of HUBEX data were brought forward. They were applied to precipitation retrieval on the Tibetan Plateau during TIPEX/IOP 1998. It was shown that the retrieval value by the PCT_{85} algorithm [Eq. (5)] was larger than the one by the SI_L algorithm [Eq. (4)] and smaller than the one by the combined SI_L and PCT_{85} algorithm [Eq. (6)]. The comparison results tell us that, on the Tibetan Plateau, the SI_L algorithm is most suitable for small rain retrieval, the PCT_{85} algorithm is most suitable for moderate rain retrieval, and the combined SI_L and PCT_{85} algorithm is most suitable for relatively large rain retrieval. By means of the two thresholds, 265 and 245 K, for TB_{85V}, the three rain-rate retrieval formulas were applied comprehensively on the Tibetan Plateau resulting in acceptable and encouraging surface RR retrieval. The intercomparison among our TMI algorithms and the 17 SSM/I algorithms from PIP-2 demonstrates that the use of the combined SI_L and PCT_{85}, tuned exclusively for the Tibetan Plateau, is advantageous over a globally developed technique. Also, the utilization of different relationships based on TB_{85V} works better than using a single method and is suitable for precipitation retrieval on the Tibetan Plateau.

Acknowledgments. The authors thank Earth Observation Research Center, NASDA, Japan, for providing the global TMI data from June to August 1998. We would also like to thank the TIPEX Group from China National Marine Environmental Forecasting Center and Peking University for providing surface precipitation data in Dangxiong. The suggestions from three anonymous reviewers also helped to improve the paper. This work is supported by the National Natural Science Foundation of China (49794030), the 1999 Science Foundation of China Meteorological Administration and Jilin Provincial Government Joint Laboratory for Weather Modification, and the National Key Program of Science and Technology of China (96-908-07-01).

REFERENCES

Chang, A. T. C., J. L. Foster, and D. K. Hall, 1990: Satellite sensor estimates of Northern Hemisphere snow volume. *Int. J. Remote Sens.*, **11,** 167–171.

Unauthenticated | Downloaded 04/24/24 07:19 AM UTC

Ferraro, R. R., and G. F. Marks, 1995: The development of SSM/I rain rate retrieval algorithms using ground based radar measurements. *J. Atmos. Oceanic Technol.,* **12,** 755–770.

——, F. Weng, N. C. Grody, and A. Basist, 1996: An eight-year (1987–1994) time series of rainfall, clouds, water vapor, snow cover, and sea ice derived from SSM/I measurements. *Bull. Amer. Meteor. Soc.,* **77,** 891–905.

Fiore, J. V., and N. C. Grody, 1992: Classification of snow cover and precipitation using SSM/I measurements: Case studies. *Int. J. Remote Sens.,* **13,** 3349–3361.

Grody, N. C., 1991: Classification of snow cover and precipitation using the Special Sensor Microwave/Imager (SSM/I). *J. Geophys. Res.,* **96,** 7423–7435.

——, and A. Basist, 1996: Global identification of snow cover using SSM/I measurements. *IEEE Trans. Geosci. Remote Sens.,* **34,** 237–249.

Kunzi, K. F., A. D. Fisher, D. H. Staelin, and J. W. Waters, 1976: Snow and ice surfaces measured by the *Nimbus 5* microwave spectrometer. *J. Geophys. Res.,* **81,** 4965–4980.

——, S. Patel, and H. Rott, 1984: Snow-cover parameters retrieved from the *Nimbus 7* scanning multichannel microwave radiometer. *Rev. Geophys.,* **22,** 452–467.

Liu, G., and J. A. Curry, 1992: Retrieval of precipitation from satellite microwave measurement using both emission and scattering. *J. Geophys. Res.,* **97,** 9959–9974.

Neale, C. M. U., M. J. McFarland, and K. Chang, 1990: Land-surface type classification using microwave brightness temperature from the Special Sensor Microwave/Imager. *IEEE Trans. Geosci. Remote Sens.,* **28,** 829–838.

Rao, P. K., and Coauthors, 1990: *Weather Satellites: Systems, Data, and Environmental Applications.* Lancaster Press, 503 pp.

Smith, E. A., and Coauthors, 1998: Results of WetNet PIP-2 project. *J. Atmos. Sci.,* **55,** 1483–1536.

Spencer, R. W., 1986: A satellite passive 37-GHz scattering-based method for measuring oceanic rain rates. *J. Climate Appl. Meteor.,* **25,** 754–766.

——, H. M. Goodman, and R. E. Hood, 1989: Precipitation retrieval over land and ocean with the SSM/I: Identification and characteristics of the scattering signal. *J. Atmos. Oceanic Technol.,* **6,** 254–273.

Unauthenticated | Downloaded 04/24/24 07:19 AM UTC